Polarimetric Backscattering Coefficients of Flooded Rice Fields at L- and C-Bands: Measurements, Modeling, and Data Analysis

Yisok Oh, *Fellow, IEEE*, Suk-Young Hong, *Member, IEEE*, Yunjin Kim, *Senior Member, IEEE*, Jin-Young Hong, *Member, IEEE*, and Yi-Hyun Kim

***Abstract*—The polarimetric backscattering coefficients (vv-, hh-, hv-, and vh-polarizations) of a flooded rice field are measured using L- and C-band ground-based polarimetric scatterometers. These measurements were made during the rice growth cycle, i.e., from the transplanting period to the harvest period (May to October 2006), to understand the feasibility of modeling and estimating rice growth. We also collected ground truth data that include fresh and dry biomasses, plant height, leaf area index, and leaf size. To study the incidence angle effect, the scatterometer data were collected at four different incidence angles, i.e., 30°, 40°, 50°, and 60°. In this paper, we show that the backscattering coefficients of a rice field can accurately be modeled using the radiative transfer theory. We also demonstrate that a polarimetric scatterometer is an effective tool for estimating rice growth. The hh-polarized backscattering coefficient is more sensitive to rice growth than its vv-polarization counterpart. The polarimetric ratio can be used to estimate rice growth accurately.**

***Index Terms*—Flooded rice field, polarimetric backscattering coefficients, radiative transfer method, scatterometer measurements.**

I. Introduction

DUE to weather conditions in the tropical monsoon climate in Asia, microwave sensors can be more effective in monitoring rice growth than optical sensors, since a longer-wavelength electromagnetic wave is less affected by clouds and precipitation events. The backscattering measurements of rice-growing areas have already been acquired using satellite synthetic aperture radars. For example, Le Toan *et al.* [1] analyzed European Remote Sensing 1 satellite (ERS-1) synthetic aperture radar (SAR) data (C-band, vv-polarization at 23°) for monitoring rice growth. They studied the ERS-1 SAR data of two rice fields to show the strong temporal variation of the radar response. The ERS-1 SAR measurements of the rice fields were compared with a theoretical model derived from the Monte Carlo simulation based on the first-order solution of the backscattering electric field. They developed a method to map a rice field based on the temporal variation of the radar response. Recently, an analysis of RADARSAT SAR data collected from rice fields was reported in [2]. The hh-polarized C-band RADARSAT data were collected at a 41° incidence angle. The dual-polarized backscattering coefficients of a rice field were collected using ENVISAT Advanced Synthetic Aperture Radar (ASAR) (5.3 GHz, hh- and hv-polarizations with incidence angles ranging from 35.8° to 39.4°) [3]. Although these satellite data were useful in assessing the scatterometer sensitivity to rice growth, they cannot be used to understand the full polarimetric responses of a rice field at various incidence angles.

In this paper, we used a fully polarimetric scatterometer to accurately measure the polarimetric (vv-, hh-, hv-, and vh-polarized) backscattering coefficients of a flooded rice field at L- and C-bands. The incidence angle varied from 30° to 60°. This ground-based scatterometer is composed of a vector network analyzer and polarimetric antenna sets at the L- and C-bands [4]. The measured data were accurately calibrated using the radar calibration techniques in [5] and [6]. For our data analysis, we used the third-order polynomial to represent the polarimetric scatterometer measurements.

The temporal variations and angular responses of the polarimetric backscattering coefficients of the rice field at the X-band have been reported in [7], where it was shown that the backscattering coefficients of the rice field at 9 GHz reach a maximum value at an early growth stage of about 43–60 days after transplanting. In this paper, we demonstrate that the L- and C-band measurements can be used to monitor the entire rice growth period. In addition, we show the feasibility of modeling the scattering mechanism of a rice field using the vector radiative transfer (VRT) method [8]. This model includes the first-order multiple scattering between the vegetation canopy and the water surface, as well as the direct backscatter from the vegetation canopy and direct backscatter from the perturbed water surface with attenuation through the vegetation canopy. To derive the input parameters of the model, we used ground truth data such as fresh and dry biomasses, plant height, leaf area index (LAI), and leaf size. The numerical results from this model compare well with the various measurements.

II. Measurements

In this paper, the rice field was located in Suwon, Korea, and kept flooded from the time of seeding until shortly before

Manuscript received April 8, 2008; revised August 14, 2008. First published April 10, 2009; current version published July 23, 2009. This work was supported in part by the Korea Agency for Defense Development through the Radiowave Detection Research Center at KAIST and in part by the KOMPSAT-5 Project of the Korea Aerospace Research Institute.

Y. Oh is with the School of Electronic and Electrical Engineering, Hongik University, Seoul 121-791, Korea (e-mail: yisokoh@hongik.ac.kr).

S.-Y. Hong and Y.-H. Kim are with the National Academy of Agricultural Science, Rural Development Administration, Suwon 441-857, Korea (e-mail: syhong@rda.go.kr; yhkim75@rda.go.kr).

Y. Kim is with the Jet Propulsion Laboratory, California Institute of Technology, Pasadena, CA 91109 USA (e-mail: yunjin.kim@jpl.nasa.gov).

J.-Y. Hong was with Hongik University, Seoul 121-791, Korea. He is now with Samsung-Thales Company, Yong-In 449-712, Korea (e-mail: nir26@hanmail.net).

Digital Object Identifier 10.1109/TGRS.2009.2014053

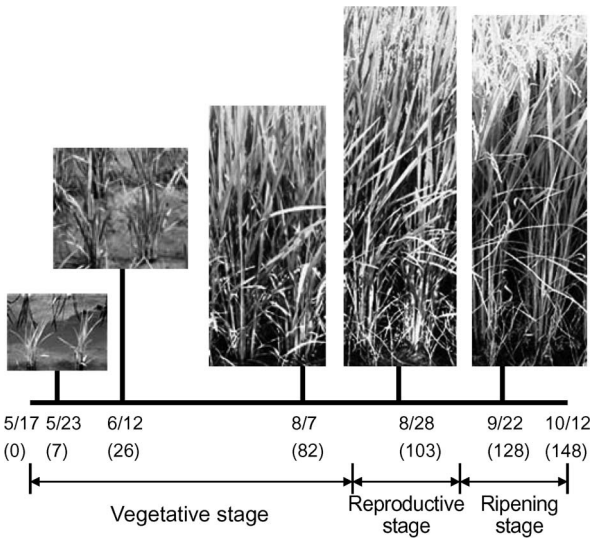

Fig. 1. Rice growth periods and rice plant clusters.

harvest. The rice seeds were sown in a nursery site on April 17, 2006. Then, the rice seedlings were transplanted in the measurement site on May 17, 2006 by using a transplanting machine. Scatterometer backscatter measurements were taken from May 29, 2006 to October 9, 2006 at the measurement site, just before the rice plants were harvested on October 12, 2006. The rice growth periods from transplant to harvest were divided into three growth stages, i.e., 1) vegetative stage from transplant to panicle initiation (about three months); 2) reproductive stage from panicle initiation to flowering (about one month); and 3) ripening stage from flowering to full maturity (about one month), as shown in Fig. 1. Fig. 1 also shows the rice plant clusters at selected dates.

We measured the vv-, hh-, hv-, and vh-polarized backscattering coefficients of the rice field at the incidence angles of 30°, 40°, 50°, and 60° with 30 independent samples at each polarization and at the incidence angle at the L- and C-bands during the rice growth cycle. The polarimetric scatterometer we used during the experiment is composed of a vector network analyzer, two polarimetric antenna sets, a laptop computer for data acquisition, and an antenna support tower. The time-gating function of the vector network analyzer was used to gate out the noise signals from antenna adapters, antenna supports, towers, and sidelobe reflection from ground. The polarimetric antenna system for the 1.9-GHz measurements consists of two orthogonally positioned R-band (1.7–2.6 GHz) standard horn antennas, whereas the antenna system for the 5.3-GHz measurements consists of an orthogonal mode transducer (OMT) and an H-band (3.9–5.9 GHz) custom-made horn antenna. The antenna systems were positioned on top of a 3.4-m tower. The scatterometer was well calibrated to get hh-, hv-, vh-, and vv-polarized backscattering coefficients from the backscatter measurements using the polarimetric calibration techniques shown in [5] and [6].

The C-band scatterometer system was precisely calibrated using the differential Mueller matrix technique (DMMT) [5], which is a rigorous calibration method for the polarimetric scatterometer measurements of distributed targets. The polarimetric responses of a calibration target over the main lobe of the antenna should be measured for this calibration technique, from which the differential Mueller matrix elements can be derived with a high degree of accuracy for characterizing radar distortion. It was proven that this technique is necessary for retrieving accurate phase-difference statistic parameters. For the backscattering coefficients (magnitude), the discrepancy between the DMMT and the single-target calibration technique (STCT) [6] was negligible (less than 1 dB), whereas the discrepancy for the phase-difference statistics was rather drastic [5].

For the DMMT, the polarimetric response of a conducting sphere was measured over the main lobe of the antenna, i.e., from -20° to $+20^\circ$ for both horizontal and vertical directions with 2° steps. The pq-polarized backscattering coefficients $(p, q = h, v)$ can be obtained from the ensemble-averaged differential Mueller matrix $\overline{\overline{M}}^0$, which can be computed from the differential correlation matrix $\overline{\overline{W}}^0$ with

$$\overline{\overline{M}}^0 = 4\pi \overline{\overline{V}}\, \overline{\overline{W}}^0 \overline{\overline{V}}^{-1} \tag{1}$$

where $\overline{\overline{V}}$ is a constant transform matrix [4]. The differential correlation matrix $\overline{\overline{W}}^0$ can be obtained from the matrix $\overline{\overline{X}}$, which has the following relation with the 4×4 correlation measurements $\overline{\overline{Y}}$ and the 4×4 correlation calibration matrix $\overline{\overline{D}}$:

$$\overline{\overline{Y}} = \overline{\overline{D}}\, \overline{\overline{X}}. \tag{2}$$

The correlation calibration matrix can be computed from the calibration procedure using the polarimetric antenna pattern, the theoretical radar cross section (RCS), and the field measurement of the calibration target [5].

The L-band scatterometer system was calibrated using the STCT [6] instead of the DMMT technique, because the polarimetric responses of a calibration target over the main lobe of the L-band antenna were not available. The STCT calibration technique is convenient and capable of correcting radar crosstalk contamination and channel imbalances by measuring the backscatter cross section of a conducting sphere or a corner reflector. The measured backscattering coefficients can be computed using the illumination integral $A_{\rm ill}$ and the calibrated true scattering matrix $\overline{\overline{S}}$ as

$$\sigma^0_{pq} = \frac{4\pi}{A_{ill,pq}} |S_{pq}|^2 \tag{3}$$

for q-polarized wave incidence and p-polarized wave scattering, where p or q denotes v or h. The true scattering matrix $\overline{\overline{S}}$ can be obtained from the scatterometer measurements $\overline{\overline{S}}_m$, inverting the following matrix equation:

$$\overline{\overline{S}}_m = \overline{\overline{R}}\, \overline{\overline{C}}\, \overline{\overline{S}}\, \overline{\overline{C}}^t\, \overline{\overline{T}} \tag{4}$$

where $\overline{\overline{R}}$, $\overline{\overline{T}}$, and $\overline{\overline{C}}$ are the receive and transmit channel imbalance matrices and the crosstalk matrix, respectively. The elements of these matrices can be obtained by the theoretical and experimental RCS of a calibration target [6]. The illumination integral could be computed using the 3-D antenna pattern,

TABLE I
MEASURED GROUND TRUTH DATA

Date	Plant total leng. (cm)	LAI	Total fresh wgt., g/cm^2	Total dry wgt., g/cm^2	Vertical hgt. (cm)	Leaf wid. (cm)	Leaf leng. (cm)
5/29	20.8	0.01	69	18	14.9	-	6.6
6/5	23.2	0.05	203	56	20.1	0.23	10.1
6/12	26.5	0.11	485	123	23.1	0.36	12.1
6/19	33.5	0.71	269	63	28.4	0.63	15.6
7/3	47.9	1.40	615	140	43.4	0.67	25.6
7/24	71.2	2.52	1160	303	58.3	-	35.5
8/7	80.9	4.63	2535	790	80.2	0.89	50.1
8/16	93.7	4.94	3245	764	86.3	0.91	54.2
8/28	96.3	5.36	3378	856	90.9	0.91	57.3
9/12	105.5	4.82	3298	1089	97.8	0.82	61.9
9/22	104.3	4.63	5255	2269	94.3	0.82	59.5
10/9	-	-	-	-	-		-

which was generated by interpolating the measured principal E- and H-plane antenna patterns.

The ground truth data of the rice field were also collected during the rice growth cycle from May 29, 2006 to October 9, 2006. The measured ground data include the rice-plant total length, LAI, fresh and dry weights, canopy vertical height, leaf width, and leaf length, as shown in Table I. Three rice clusters were selected for measuring the ground data. The rice leaves were detached from the stems and used to measure the total areas using LI-3100 (LI-COR, Inc.), and the LAI was computed using the density of the rice clusters. The dry biomasses were measured by drying the vegetation particles in a dryer at 80 °C for 48 h.

III. MODELING

The VRT theory is a common technique for computing polarimetric microwave scattering from randomly distributed scatterers [8]. In this paper, the rice field is modeled as a vegetation canopy consisting of randomly distributed lossy dielectric thin leaves over a water surface for applying the first-order VRT method. The water surface had slightly been perturbed by various floating materials, protruding soil bumps, and even by winds at the early growing stages. Thus, the microwave backscattering from this vegetation canopy comprises the following five main scattering mechanisms for the first-order RT model, as shown in Fig. 2: 1) direct backscattering from the vegetation canopy layer (I–V–S); 2) forward scattering from the vegetation layer and then reflecting from the water surface (I–V–W–S); 3) reflecting from the water surface and then forward scattering from the vegetation layer (I–W–V–S); and 4) reflecting from the water surface, then backscattering from the vegetation layer, and reflecting again from the water surface (I–W–V–W–S); and 5) direct backscattering from the perturbed water surface with two-way attenuations through the vegetation layer (I–W–S).

The backscattering coefficients can be obtained by multiplying $4\pi\cos\theta_0$ to the transformation matrix elements, e.g., $\sigma^o_{vv} = 4\pi\cos\theta_0 T_{11}$ and $\sigma^o_{vh} = 4\pi\cos\theta_0 T_{12}$. The 4×4 transformation matrix $\overline{\overline{T}}$ can be computed using the phase matrix $\overline{\overline{P}}$, the eigen matrix $\overline{\overline{E}}$, the reflectivity matrix $\overline{\overline{R}}$, the diagonal

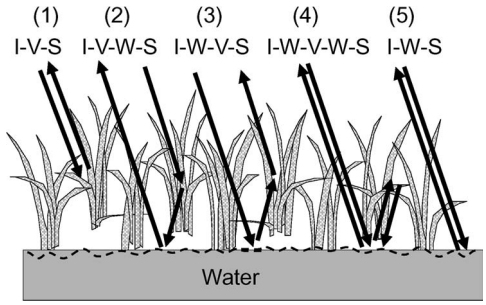

Fig. 2. Five main scattering mechanisms.

extinction matrix $\overline{\overline{D}}$, and the Stokes scattering operator matrix $\overline{\overline{M}}$ [4], [8] as

$$\begin{aligned}\overline{\overline{T}} = \sec\theta_0 \Bigg[& \overline{\overline{E}}_4\, \overline{\overline{A}}_{41}\, \overline{\overline{E}}_1^{-1} + \left\{\overline{\overline{E}}_4 \overline{\overline{D}}_4 \overline{\overline{E}}_4^{-1}\right\} \overline{\overline{R}}\, \overline{\overline{E}}_3\, \overline{\overline{A}}_{31}\, \overline{\overline{E}}_1^{-1} \\ & + \overline{\overline{E}}_4\, \overline{\overline{A}}_{42}\, \overline{\overline{E}}_2^{-1} \overline{\overline{R}} \left\{\overline{\overline{E}}_1 \overline{\overline{D}}_1 \overline{\overline{E}}_1^{-1}\right\} + \left\{\overline{\overline{E}}_4 \overline{\overline{D}}_4 \overline{\overline{E}}_4^{-1}\right\} \\ & \times \overline{\overline{R}}\, \overline{\overline{E}}_3\, \overline{\overline{A}}_{32}\, \overline{\overline{E}}_2^{-1} \overline{\overline{R}} \left\{\overline{\overline{E}}_1 \overline{\overline{D}}_1 \overline{\overline{E}}_1^{-1}\right\} \\ & + \left\{\overline{\overline{E}}_4 \overline{\overline{D}}_4 \overline{\overline{E}}_4^{-1}\right\} \overline{\overline{M}} \left\{\overline{\overline{E}}_1 \overline{\overline{D}}_1 \overline{\overline{E}}_1^{-1}\right\} \Bigg] \end{aligned} \tag{5}$$

with

$$[\overline{\overline{A}}_{kl}]_{ij} = \left[\overline{\overline{E}}_k^{-1} \overline{\overline{P}}_{kl} \overline{\overline{E}}_l\right]_{ij} C_{kl,ij}. \tag{6}$$

The first, second, third, fourth, and fifth terms of the foregoing equation correspond to scattering mechanisms 1 (I–V–S), 2 (I–V–W–S), 3 (I–W–V–S), 4 (I–W–V–W–S), and 5 (I–W–S) in Fig. 2, respectively. The subscripts 1, 2, 3, and 4 correspond to the directions of incidence downward ($\searrow$), incidence (or scattering) upward ($\nearrow$), scattering (or incidence) downward ($\swarrow$), and scattering upward ($\nwarrow$), respectively. In (6), the subscripts k and l denote the wave directions, and the subscripts i and j denote the ijth element of the matrix.

The wave attenuation through the vegetation canopy is accounted for using Foldy's approximation [8]. The diagonal terms of the diagonal matrices $\overline{\overline{D}}$ can be obtained from the eigen values β_i of coherent propagation. The elements of the associate eigen matrix $\overline{\overline{E}}$, as well as the eigen values β_i, can be computed from the elements of the averaged scattering matrix $\overline{\overline{B}}$ [8] as

$$\overline{\overline{B}} = \left\langle \overline{\overline{S}}(\theta,\phi;\theta,\phi) \right\rangle j2\pi N/k. \tag{7}$$

The constant $C_{kl,ij}$ in (6) can be summarized as

$$C_{41,ij} = \frac{1 - e^{[-\{\beta_i(\theta_s,\phi_s)\sec\theta_s + \beta_j(\pi-\theta_0,\phi_i)\sec\theta_0\}d]}}{\beta_i(\theta_s,\phi_s)\sec\theta_s + \beta_j(\pi-\theta_0,\phi_i)\sec\theta_0} \tag{8}$$

$$C_{31,ij} = \frac{e^{[-\beta_i(\pi-\theta_s,\phi_s)d\sec\theta_s]} - e^{[-\beta_j(\pi-\theta_0,\phi_i)d\sec\theta_0]}}{-\beta_i(\pi-\theta_s,\phi_s)\sec\theta_s + \beta_j(\pi-\theta_0,\phi_i)\sec\theta_0}. \tag{9}$$

$C_{32,ij}$ can be computed from $C_{41,ij}$ with substitutions of $(\pi - \theta_s, \phi_s)$ into (θ_s, ϕ_s) and (θ_0, ϕ_i) into $(\pi - \theta_0, \phi_i)$, and $C_{42,ij}$

can be computed from $C_{31,ij}$ with substitutions of (θ_s, ϕ_s) into $(\pi - \theta_s, \phi_s)$ and (θ_0, ϕ_i) into $(\pi - \theta_0, \phi_i)$.

The reflectivity matrix can be computed using the Fresnel reflection coefficients with a modification for a rough surface by multiplying the physical optics (PO) modification factor

$$R_p = |\Gamma_p|^2 e^{-(2ks\cos\theta)^2} \tag{10}$$

where Γ_p is the Fresnel reflection coefficient for p-polarization ($p = v$ or h), s is the RMS height, k is the wavenumber, and θ is the incidence angle. The phase matrix is the average of the Mueller matrix over the distribution of particles in terms of size, shape, and orientation, where the Mueller matrix elements are the covariance between the scattering matrix elements [8].

A rice leaf is modeled as a lossy dielectric thin rectangular disk for simplicity. It was shown in [9] that the RCS of a thin leaf can alternatively be computed by either the PO model or the generalized Rayleigh–Gans (GRG) model at microwave frequencies. In this paper, the scattering matrices for the rice leaves were computed using the PO model and the resistive sheet approximation. The scattering matrix element for pq-polarization S_{pq} is $\hat{p}_s \cdot \overline{\overline{S}} \cdot \hat{q}_i$, where the scattering matrix field $\overline{\overline{S}}$ is defined as

$$\overline{E}^s(\overline{r}) = \frac{e^{ikr}}{r}\overline{\overline{S}}(\hat{k}_s, \hat{k}_i) \cdot \hat{q}_i E_0 \tag{11}$$

and computed from the equivalent current distribution on the rice leaves. The equivalent current $\overline{J}(\overline{r}')$ can be approximated to a surface current distribution $\overline{J}_s^R(\overline{r}')$ on the resistive sheet as

$$\overline{J}_s^R(\overline{r}') = \overline{J}_s^{\mathrm{pc}}(\overline{r}')\,\Gamma_q \tag{12}$$

where $\overline{J}_s^{\mathrm{pc}}(\overline{r}')$ is the PO surface current on a perfect conductor, Γ_q is the reflection coefficient for a resistive sheet at q-polarization, which is given in [10] as

$$\Gamma_h = \left[1 + \frac{2R_l\cos\theta_0}{\eta_0}\right]^{-1} \qquad \Gamma_v = \left[1 + \frac{2R_l}{\eta_0\cos\theta_0}\right]^{-1} \tag{13}$$

with the resistivity of the leaf $R_l = i\eta_0/k_0 t(\varepsilon_r - 1)$, where $\theta_0 = \pi - \theta_i$, and t is the leaf thickness. The relative permittivity ε_r of a rice leaf has been computed by the empirical formula in [11] using the gravimetric water content of the leaf.

We tried to retrieve the roughness parameters of the perturbed water surface from the scatterometer measurements because the radar backscatter is dominated by surface scattering for a very sparse vegetation canopy. The polarimetric radar measurements on June 5, 2006 at the L- and C-bands were fitted with the model to estimate the RMS height s and the correlation length l using the minimum mean square error (MMSE) technique. In this model, we employed the small perturbation method (SPM) for surface scattering with the dielectric constants (79.18, -8.23) at 1.9 GHz and (73.54, -21.20) at 5.3 GHz for the water surface [11]. It was found that the measurements and model outputs agree quite well with the RMS height $s = 0.1$ cm and the correlation length $l = 2$ cm for the surface. We used these estimated surface roughness parameters for all the other rice fields.

TABLE II
INPUT PARAMETERS FOR THE MODEL

Date	Days after transplant	Canopy height (cm)	Leaf wid. (cm)	Leaf leng. (cm)	Leaf dens. (cm^{-3})	Grav. water cont. (g/g)
5/29	12	16.0	0.22	6.9	168	0.74
6/5	19	18.9	0.32	9.1	298	0.74
6/12	26	23.2	0.41	12.1	419	0.74
6/19	33	28.5	0.50	15.8	531	0.74
7/3	47	41.4	0.65	24.5	724	0.75
7/24	68	63.4	0.82	39.1	934	0.75
8/7	82	77.3	0.88	48.2	1016	0.75
8/16	91	84.9	0.91	53.2	1043	0.75
8/28	103	92.6	0.91	58.3	1044	0.73
9/12	118	96.7	0.86	61.0	987	0.70
9/22	128	95.0	0.79	60.1	913	0.68
10/9	145	82.1	0.62	52.0	713	0.61

The major input parameters of the model are canopy height, distributions of leaf sizes and orientations, leaf density, and water contents of rice leaves. The leaf density was computed from the measured LAI and the measured leaf width and length for each measurement, and the gravimetric water content was computed from the measured fresh and dry weight in Table I. It was found that the measured ground data fluctuated date by date. Therefore, the input parameters, such as canopy height, leaf width, leaf length, leaf density, and water content, were obtained from the polynomial regression of the measured ground data, as shown in Table II. The distribution of the leaf orientation was assumed to be uniform for vertical and horizontal directions in the range of $0 \le \theta \le \pi/2, 0 \le \varphi \le 2\pi$. The distributions of the leaf widths and lengths were also assumed to be uniform in appropriate ranges with the measured mean values. The leaf thickness of 0.5 mm was used for all cases in this model computation.

The reduction of the scattering amplitude for a curved leaf is included in this model with the following relation [10]:

$$S = S_{fp}\left(\frac{b}{2}\sqrt{\frac{k}{\rho}}\right)^{-1} F\left(\frac{b}{2}\sqrt{\frac{k}{\rho}}\right) \tag{14}$$

where S is the scattering amplitude, the subscript fp stands for "flat plate," b is the length of a leaf, ρ is the radius of the curvature, and F is the Fresnel integral defined by

$$F(\tau) = \int_0^{\tau} e^{-ju^2} du. \tag{15}$$

The Fresnel integral can be approximated by $0.5\sqrt{\pi}\exp[-j\pi/4]$ for a large argument. In this paper, the radius of 12.7 b^2 was selected by comparing between the measurements and the model outputs for Data-6 (measurements on July 24, 2006) using the MMSE technique. The reduction of the scattering amplitude is negligible at the L-band and about 40% at the C-band with the radius.

Fig. 3(a)–(c) shows the contributions of the five scattering mechanisms for vv-, hh-, and hv-polarizations, respectively, for the measurements on June 5, 2006 (Data-2) at L-band.

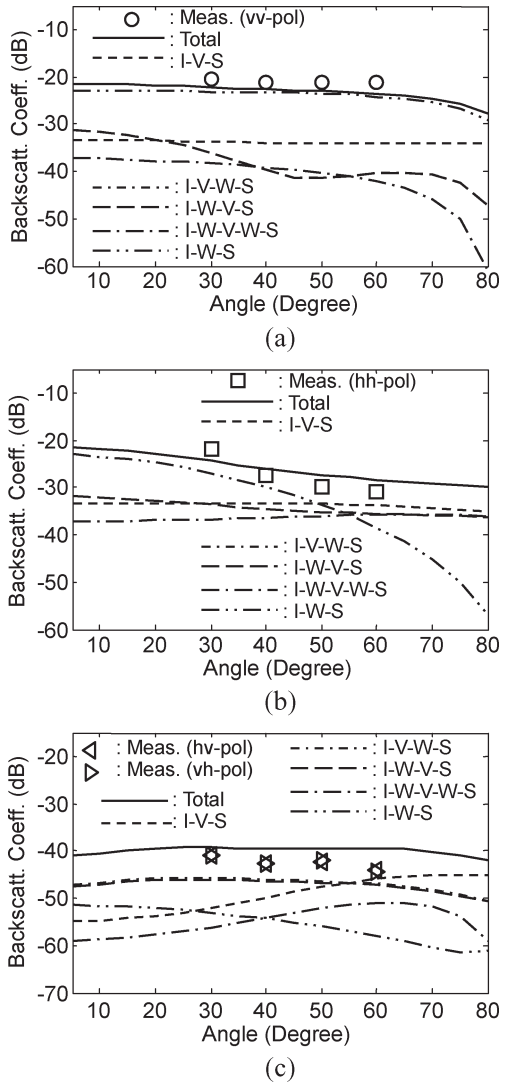

Fig. 3. Contributions of the five scattering mechanisms for Data-2 (June 5, 2006) at the L-band for (a) vv-, (b) hh-, and (c) hv-polarizations.

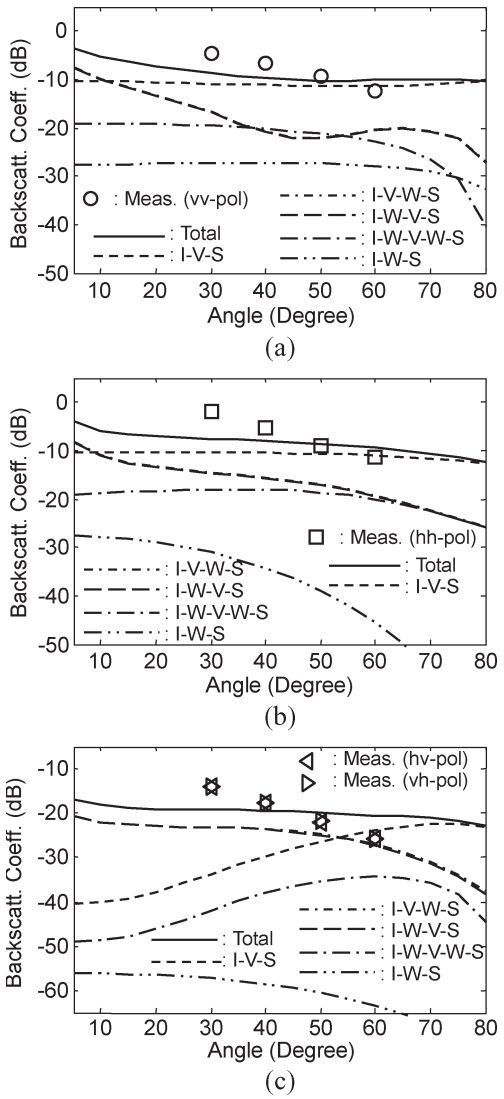

Fig. 4. Contributions of the five scattering mechanisms for Data-8 (August 16, 2006) at the L-band for (a) vv-, (b) hh-, and (c) hv-polarizations.

The direct scattering from the perturbed water surface (I–W–S) is dominant for the vv-polarized backscattering coefficients, as shown in Fig. 3(a), because the rice field on June 5 had a very sparse vegetation canopy. For the hh-polarization, however, the I–W–S mechanism was only dominant at lower incidence angles ($\theta < 45^\circ$), as shown in Fig. 3(b), because of the lower surface scattering for hh-polarization at higher incidence angles. The scattering mechanisms 2 and 3 (I–V–W–S and I–W–V–S) were higher than the other scattering mechanisms for cross polarization at the lower incidence angles, as shown in Fig. 3(c), because of the specular forward scattering in the scattering mechanisms 2 and 3.

Fig. 4(a)–(c) shows the contributions of the five scattering mechanisms for vv-, hh-, and hv-polarizations, respectively, for the L-band measurements on August 16, 2006 (Data-8). In this case, the direct scattering from the water surface (I–W–S) was negligible because of the higher attenuation in the dense vegetation canopy. Instead, the direct scattering from the vegetation canopy (I–V–S) was dominant for the copolarized backscattering coefficients because of the higher density of the leaves. The multiple scattering between the vegetation canopy and the water surface (I–V–W–S and I–W–V–S) was dominant for the cross polarization at $\theta < 55^\circ$ because of the higher specular forward scatter than the backscatter for the cross polarization.

Fig. 5(a) and (b) shows the comparison between the measured and estimated temporal variations of the backscattering coefficients at 40° in the L- and C-bands, respectively, for the whole growth period. The temporal polarimetric backscattering coefficients have been estimated using the input parameters in Table II. The model estimation agrees relatively well with the measured backscattering coefficients for both frequencies.

IV. Data Analysis

We first analyzed the temporal variations of the measured polarimetric backscattering coefficients. Fig. 6 shows the vv-, hh-, hv-, and vh-polarized backscattering coefficients of the rice field at 5.3 GHz and 30°. The vv-polarized backscattering coefficients only increased at the vegetative stage, were saturated at the reproductive stage, and even decreased at the

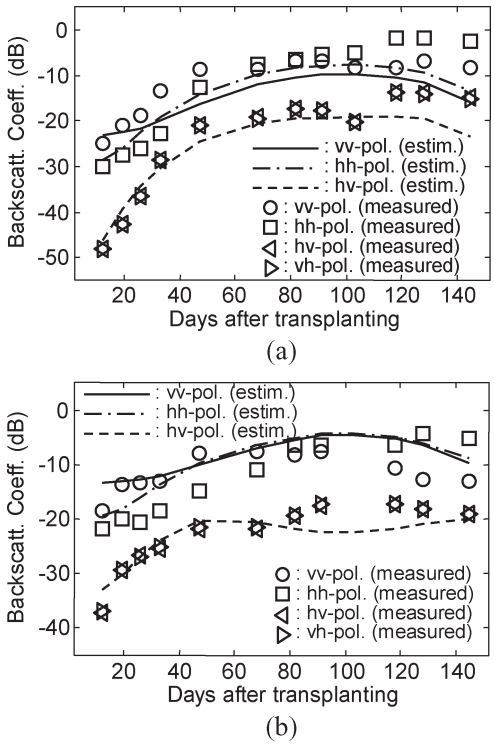

Fig. 5. Comparison between the measured and estimated backscattering coefficients at 40° for the whole rice growth period at the (a) L- and (b) C-bands.

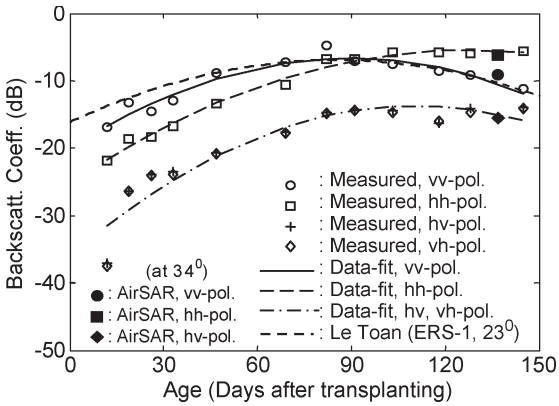

Fig. 6. Comparison between the scatterometer data, the ERS-1 data in [1], and the AirSAR data at 5.3 GHz and 30°.

ripening stage due to the canopy attenuation, whereas the hh-polarized responses increased even at the reproductive stage and were saturated at the ripening stage. The temporal trend of the cross-polarized backscattering coefficients follows the hh-polarization. Fig. 6 also shows the temporal variation of the ERS-1 data (23°) in [1], which represent the data-fit curve $(y = -0.001265x^2 + 0.2919x - 23.758)$ for the Akita and Semarang test sites. The temporal trend and the absolute level of the ERS-1 data agree quite well with the scatterometer data. Fig. 6 also shows the JPL/AirSAR measurements at 34° for a rice field at Non-San, Korea, during the PACRIM-2 campaign on September 30, 2000. The AirSAR polarimetric measurement also agrees well with the scatterometer measurements.

Fig. 7(a) and (b) shows, respectively, the C-band polarimetric backscattering coefficients of the rice field at the incidence

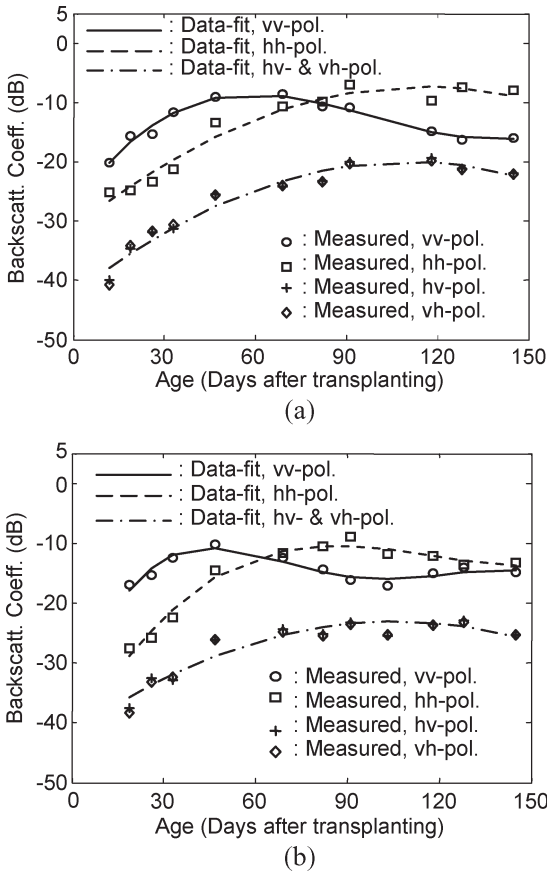

Fig. 7. Measured polarimetric backscattering coefficients at 5.3 GHz at (a) 50° and (b) 60°.

angles of 50° and 60°. The vv-polarized backscattering coefficients reach the peak values earlier than the hh-polarized responses at all incidence angles. For example, the vv-polarized backscattering coefficients at 60° reach the peak value quite early, even at about 40–50 days after transplanting [Fig. 7(b)], because of high attenuation at a higher incidence angle due to a longer wave path than a lower incidence angle. We can conclude that the hh-polarized backscattering coefficients are more sensitive to growth age than the vv-polarized responses. Fig. 8(a) and (b) shows the temporal polarimetric responses to the flooded rice field at 1.9 GHz at 30° and 50°. The temporal trends at 1.9 GHz are quite similar to those at 5.3 GHz, except that the temporal L-band backscatters reach peak values later than those at the C-band because of the lower effective density (correspondingly, the lower attenuation) at the L-band. For example, the peak of the vv-polarized response at 30° occurs at about the 80-day age at the C-band and at about the 120-day age at the L-band, as shown in Figs. 6 and 8(a). All the temporal measurements of the vv-, hh-, vh-, and hv-polarized backscattering coefficients at 30°, 40°, 50°, and 60° at the C- and L-bands are regressed with third-order polynomials, and the coefficients of the regressed third-order polynomials are given in Table III.

Considering the polarimetric responses at 30°, as shown in Fig. 6, it can be noticed that the vv-polarized response is higher than the hh-polarized response when the surface scattering is dominant for relatively sparse vegetation canopies at the early

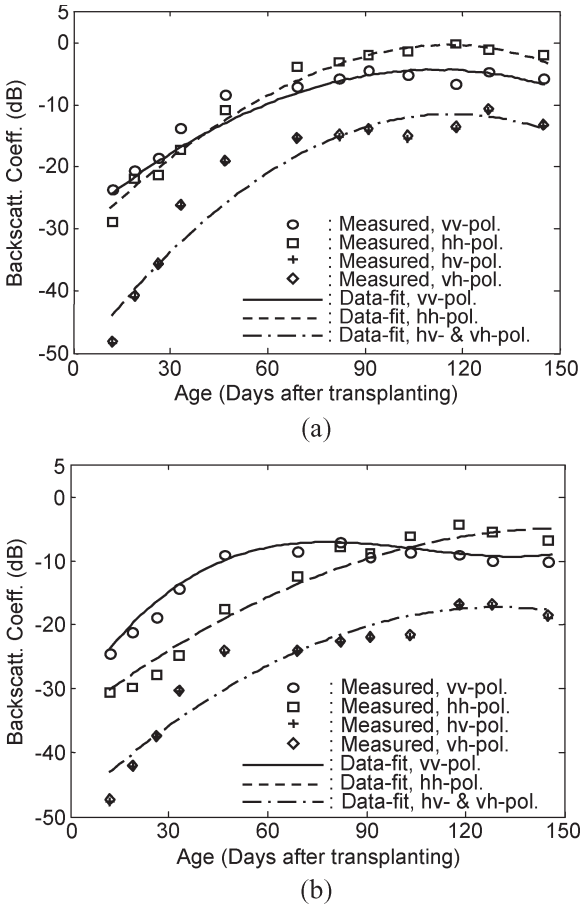

Fig. 8. Measured polarimetric backscattering coefficients at 1.9 GHz at (a) 30° and (b) 50°.

TABLE III
POLYNOMIAL COEFFICIENTS FOR THE REGRESSION DATA FIT

Freq.	θ	Pol.	$\sigma^0=ax^3+bx^2+cx+d$ (dB) (x=day after transplanting)			
			a	b	c	d
5.3 GHz	30	VV	0	-0.0017	0.301	-20.10
		HH	0	-0.0012	0.311	-25.21
		VH, HV	0	-0.0019	0.409	-36.21
	40	VV	0	-0.0018	0.301	-20.08
		HH	0	-0.0012	0.321	-26.68
		VH, HV	0	-0.0018	0.381	-37.30
	50	VV	3.03e-5	-0.0090	0.755	-27.96
		HH	0	-0.0018	0.416	-31.41
		VH, HV	0	-0.0019	0.410	-42.59
	60	VV	3.33e-5	-0.0085	0.615	-25.41
		HH	2.45e-5	-0.0088	0.966	-44.29
		VH, HV	0	-0.0017	0.356	-41.85
1.9 GHz	30	VV	2.02e-5	-0.0069	0.757	-32.45
		HH	0	-0.0027	0.601	-34.15
		VH, HV	0	-0.0035	0.767	-52.84
	40	VV	2.60e-5	-0.0083	0.834	-34.01
		HH	0	-0.0022	0.562	-37.36
		VH, HV	0	-0.0030	0.672	-52.09
	50	VV	2.72e-5	-0.0086	0.845	-34.06
		HH	0	-0.0022	0.538	-38.90
		VH, HV	0	-0.0023	0.549	-50.33
	60	VV	2.62e-5	-0.0090	0.870	-34.84
		HH	0	-0.0023	0.535	-40.32
		VH, HV	0	-0.0025	0.533	-52.28

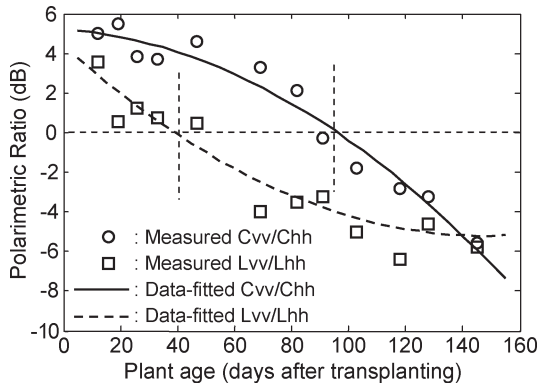

Fig. 9. Measured polarimetric ratios at 30°; Cvv/Chh and Lvv/Lhh.

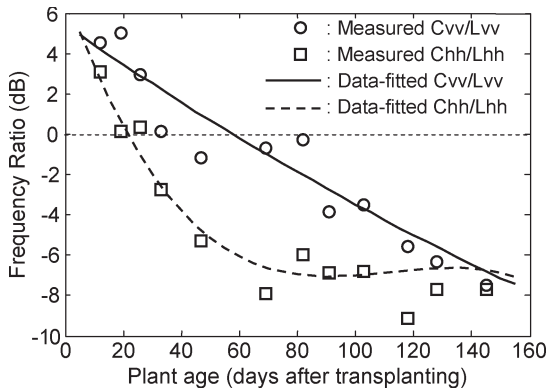

Fig. 10. Measured frequency ratios at 30°; Cvv/Lvv and Chh/Lhh.

season. On the other hand, the hh-polarized response is higher than the vv-polarized response for relatively dense vegetation canopies at a late growing season because of less attenuation for hh-polarization than vv-polarization due to the canopy geometry and the double bounce component. The dynamic range of the hh-polarized backscattering coefficients at 30° during the rice growth cycle is about 16.2 dB (−21.9 to −5.7 dB), which is much higher than the range for vv-polarization, which is about 10.1 dB (−16.9 to −6.8 dB). Therefore, the hh-polarized backscattering coefficient has a wider temporal sensitivity than the vv-polarized backscattering coefficient.

Fig. 9 shows the polarimetric ratios $(\sigma^0_{vv}/\sigma^0_{hh})$ at 30° at the C- and L-bands (Cvv/Chh and Lvv/Lhh). The polarimetric ratios are sensitive to rice plant age because of the differential scattering mechanisms and attenuation depending on the incidence wave polarization (more attenuation for vertical polarization as the rice canopies grow). The polarimetric ratios decrease from 5 to −6 dB for both frequencies. In other words, the increase rate of the backscattering coefficient for hh-polarization is much larger than that for vv-polarization. The hh-polarized response crosses over the vv-polarized response at about 95 days at the C-band and at about 40 days after transplanting at the L-band, as shown in Figs. 6, 8(a), and 9.

Fig. 10 shows the frequency ratios for both hh- and vv-polarizations (Cvv/Lvv and Chh/Lhh), and also shows that the backscattering coefficients at the C-band are lower at the latter part of the rice-growing season, because the wave cannot penetrate into the vegetation canopy in a dense rice field such that the water-bounce scattering at the C-band is negligible.

On the other hand, the backscattering coefficients at the C-band are higher at the first part of the rice-growing season because of the higher effective surface roughness at the C-band. The sensitivities of the polarimetric and frequency ratios at 40° are quite similar to those at 30°, but the differences between the L- and the C-bands and between the vv- and hh-polarizations are lesser than those shown in Figs. 9 and 10.

V. Concluding Remark

The vv-, hh-, hv-, and vh-polarized backscattering coefficients of a flooded rice field were precisely measured using L- and C-band ground-based polarimetric scatterometers at 30°, 40°, 50°, and 60°. These scatterometer measurements and the ground truth data collections were made during the rice growth cycle from May to October 2006 to understand the feasibility of modeling and estimating rice growth. We have shown that the backscattering coefficients of a rice field can be modeled using the radiative transfer theory. We have also demonstrated that a well-calibrated polarimetric scatterometer is an effective tool for estimating rice growth. The hh-polarized backscattering coefficient is more sensitive to rice growth than its vv-polarization counterpart. It has also been shown that the polarimetric and frequency ratios are sensitive to the rice plant age.

Acknowledgment

The authors would like to thank G. Jang (Hongik University) for his help in the data acquisition and the reviewers for their thorough reading of the manuscript and their constructive comments.

References

[1] T. Le Toan, F. Ribbes, L.-F. Wang, N. Floury, K.-H. Ding, J. A. Kong, M. Fujita, and T. Kurosu, "Rice crop mapping and monitoring using ERS-1 data based on experiment and modeling results," *IEEE Trans. Geosci. Remote Sens.*, vol. 35, no. 1, pp. 41–56, Jan. 1997.

[2] J.-Y. Koay, C.-P. Tan, K.-S. Lim, S. B. A. Bakar, H.-T. Ewe, H.-T. Chuah, and J. A. Kong, "Paddy fields as electrically dense media: Theoretical modeling and measurement comparisons," *IEEE Trans. Geosci. Remote Sens.*, vol. 45, no. 9, pp. 2837–2849, Sep. 2007.

[3] J. Chen, H. Lin, and Z. Pei, "Application of ENVISAT ASAR data in mapping rice crop growth in Southern China," *IEEE Geosci. Remote Sens. Lett.*, vol. 4, no. 3, pp. 431–435, Jul. 2007.

[4] F. T. Ulaby and C. Elachi, *Radar Polarimetry for Geoscience Applications*. Norwood, MA: Artech House, 1990.

[5] K. Sarabandi, Y. Oh, and F. T. Ulaby, "Measurement and calibration of differential Mueller matrix of distributed targets," *IEEE Trans. Antennas Propag.*, vol. 40, no. 12, pp. 1524–1532, Dec. 1992.

[6] K. Sarabandi and F. T. Ulaby, "A convenient technique for polarimetric calibration of single-antenna radar systems," *IEEE Trans. Geosci. Remote Sens.*, vol. 28, no. 6, pp. 1022–1033, Nov. 1990.

[7] S. Kim, B. Kim, Y. Kong, and Y.-S. Kim, "Radar backscattering measurements of rice crop using X-band scatterometer," *IEEE Trans. Geosci. Remote Sens.*, vol. 38, no. 3, pp. 1467–1471, May 2000.

[8] L. Tsang, J. A. Kong, and R. T. Shin, *Theory of Microwave Remote Sensing*, 1st ed. Hoboken, NJ: Wiley, 1985.

[9] Y. Oh and J. Y. Hong, "Re-examination of analytical models for microwave scattering from deciduous leaves," *IET Microw., Antennas, Propag.*, vol. 1, no. 3, pp. 617–623, Jun. 2007.

[10] K. Sarabandi, T. B. A. Senior, and F. T. Ulaby, "Effect of curvature on the backscattering from leaves," *J. Electromagn. Waves Appl.*, vol. 2, no. 7, pp. 658–670, 1988.

[11] F. T. Ulaby, M. K. Moore, and A. K. Fung, *Microwave Remote Sensing, Active and Passive*, vol. 3. Norwood, MA: Artech House, 1986.

Yisok Oh (S'88–M'94–SM'03–F'09) received the B.S. degree in electrical engineering from Yonsei University, Seoul, Korea, in 1982, the M.S. degree in electrical engineering from the University of Missouri-Rolla, in 1988, and the Ph.D. degree in electrical engineering from the University of Michigan, Ann Arbor, in 1993.

Since 1994, he has been with the School of Electronic and Electrical Engineering, Hongik University, Seoul, where he is currently a Professor. His research interests include microwave remote sensing, antennas, and radio wave propagation.

Suk-Young Hong (M'09) received the B.S., M.S., and Ph.D. degrees from Kyungpook National University, Daegu, Korea, in 1990, 1992, and 1999, respectively, all in agronomy.

She is currently a Senior Research Scientist with the Department of Agricultural Environment, National Academy of Agricultural Science, Rural Development Administration, Suwon, Korea. Her research interests include the agricultural application of remote sensing, soil and environment informatics, and pedometrics.

Yunjin Kim (S'86–M'87–SM'99) received the Ph.D. degree from the University of Pennsylvania, Philadelphia, in 1987.

From 1987 to 1989, he was an Assistant Professor with the Department of Electrical Engineering, New Jersey Institute of Technology, Newark. Since 1989, he has been with the Jet Propulsion Laboratory, California Institute of Technology, Pasadena, where he is currently the NuSTAR Project Manager. His research interests include radar polarimetry and interferometry, radar system engineering, soil moisture algorithm development, radar system engineering, and advanced radar technology development.

Jin-Young Hong (S'06–M'09) received the B.S., M.S., and Ph.D. degrees from Hongik University, Seoul, Korea, in 2000, 2002, and 2008, respectively, all in radio science and communication engineering.

From 2002 to 2003, he was with the Samsung Electro-mechanics Company, Suwon, Korea. Since 2008, he has been with the Samsung-Thales Company, Yong-In, Korea, where he works on the development of radar systems. His current research interests include radar systems and remote sensing.

Yi-Hyun Kim received the B.S. degree in agricultural chemistry from Daegu University, Gyeongsan, Korea, in 2000 and the M.S. degree in agricultural chemistry from Seoul National University, Seoul, Korea, in 2002.

He is currently a Research Scientist with the Department of Agricultural Environment, National Academy of Agricultural Science, Rural Development Administration, Suwon, Korea. His research interests include the agricultural application of microwave remote sensing and GIS.